

Targeting C99-Mediated Metabolic Disruptions with Ketone Therapy in Alzheimer's Disease

Hao Huang,¹, Kaijing Xu¹ and Michael Lardelli¹

Abstract

The role of ketone bodies in Alzheimer's disease (AD) remains incompletely understood, particularly regarding their influence on amyloid pathology. While β -hydroxybutyrate (BHB) has been implicated in neuroprotection, direct evidence for its effects on amyloid- β (A β) deposition, aggregation, or clearance is lacking. Furthermore, whether BHB acts as a disease-modifying factor or merely confers transient metabolic benefits remains unclear. Addressing this gap is crucial for evaluating the therapeutic potential of ketone metabolism in AD. Here, we investigated the impact of ketone bodies on amyloidogenic toxicity using a *Drosophila melanogaster* model with targeted expression of human amyloid precursor protein (APP), β -secretase 1 (BACE1), A β , and the C99 fragment—an essential intermediate in A β generation. Surprisingly, we found that A β alone elicited minimal neurotoxicity, whereas C99 expression induced pronounced pathological effects, suggesting a critical, underappreciated role of C99 in AD progression. Further analysis revealed that C99-driven toxicity was associated with autophagic and lysosomal dysfunction, leading to impaired protein clearance, oxidative stress, and mitochondrial abnormalities. Using confocal microscopy and lysosomal pH-sensitive markers, we demonstrated that BHB treatment restored lysosomal function and alleviated these pathological changes. Protein–protein interaction network analysis in C99-expressing *Drosophila* brains identified protein phosphatase methylesterase-1 (PPME1) activation as a key driver of autophagic impairment, further supported by machine learning predictions. Finally, mathematical similarity analysis of PPI networks suggested that BHB may exert its neuroprotective effects through mTOR inhibition, positioning it as a potential endogenous modulator of AD-related pathology. These findings highlight a previously unrecognized pathogenic role of C99 in AD and provide mechanistic insights into BHB-mediated neuroprotection, supporting the therapeutic potential of ketone metabolism in neurodegenerative diseases.

Author affiliations:

1 Faculty of Sciences, Engineering and Technology, University of Adelaide, North Terrace, Adelaide, 5005, SA, Australia.

Correspondence to: Hao Huang

Full address: Gate8 Victoria Dr, The University of Adelaide Adelaide, North Terrace, SA5005, Australia

E-mail: hao.huang01@adelaide.edu.au

Running title: Inhibition of protein interaction of C99 by BHB

Keywords: Alzheimer's disease; β -Hydroxybutyrate (BHB); C99; Proteostasis

Introduction

Alzheimer's disease (AD) is a severe neurodegenerative disorder characterized by progressive cognitive decline and neuronal loss¹. One of the hallmark pathological features of AD is the aberrant accumulation of neurotoxic protein aggregates, which not only serve as critical biomarkers of disease progression but also directly mediate neuronal dysfunction and cell death. Among these, amyloid- β (A β) and tau proteins have garnered significant attention due to their pivotal roles in AD pathogenesis². Abnormal A β aggregation induces synaptic dysfunction, mitochondrial impairment, and neuroinflammation, while excessive tau phosphorylation disrupts microtubule integrity, thereby exacerbating neurodegeneration³.

Beyond these well-established pathological markers, emerging evidence suggests that intermediate cleavage products of amyloid precursor protein (APP), such as C99, as well as proteins involved in proteostasis, autophagy, and lysosomal function, also contribute to AD onset and progression^{4,5}. Dysregulation of these proteins can lead to impaired proteostasis, aberrant cellular signaling, and defective protein clearance mechanisms, thereby intensifying neurotoxicity and cognitive deficits^{6,7}.

Despite various therapeutic strategies aimed at mitigating the impact of toxic protein aggregation, recent studies suggest that metabolic interventions may modulate the underlying disease pathology. Ketone bodies (KBs), including β -hydroxybutyrate (BHB), acetoacetate (AcAc), and acetone, are small, lipid-derived molecules produced in the liver through fatty acid oxidation, primarily during fasting, prolonged exercise, or carbohydrate restriction^{8,9}. As

alternative energy substrates, KBs can cross the blood-brain barrier and serve as a crucial energy source for neurons when glucose availability is limited. In addition to their metabolic role, KBs have been implicated in modulating various cellular processes^{8,10,11}. Among KBs, BHB has been proposed as a potential neuroprotective regulator in AD. Recent findings indicate that BHB modulates autophagy via the SIRT1 signaling pathway, facilitating the degradation and clearance of AD-associated toxic proteins^{10,12}. Moreover, BHB has been shown to restore autophagic flux and mitigate glucose deprivation-induced neurotoxicity^{13–15}. In addition, BHB suppresses the activation of the NLRP3 inflammasome, thereby reducing neuroinflammation and ameliorating AD pathology^{16–18}. One proposed mechanism is its ability to enhance mitochondrial ATP production through β -hydroxybutyrylation of key enzymes in the tricarboxylic acid (TCA) cycle, thereby alleviating energy deficits that exacerbate A β toxicity^{19,20}. Additionally, BHB modulates neuroinflammation by activating G protein-coupled receptor 109A (GPR109A), shifting microglia toward a neuroprotective phenotype, which may indirectly reduce A β -induced neurotoxicity²¹. However, there is no evidence that BHB directly modulates A β deposition, aggregation, or clearance, nor does it appear to influence the amyloidogenic processing of APP. Given the central role of lipid metabolism in neuronal homeostasis, it remains unclear whether BHB acts as a disease-modifying factor or merely provides transient neuroprotection. Addressing this gap will be essential for determining the therapeutic potential of ketone metabolism in AD.

This study aims to determine whether ketone bodies can mitigate the toxicity of key biomarker proteins in the amyloidogenic pathway and elucidate the underlying mechanisms. Understanding this relationship could provide critical insights into the potential role of ketone metabolism in modifying neurodegenerative disease progression and inform novel therapeutic strategies for AD. To address this question, we utilized the flexible UAS-GAL4 expression system in *Drosophila melanogaster* to express human APP, β -secretase 1 (BACE1), A β , and the C99 fragment—an intermediate precursor of A β —in the fly eye²². Our findings indicate that A β alone, commonly considered neurotoxic, exhibits limited damage in this model, whereas the presence of C99 is required for substantial pathological effects. Based on existing literature and the observation of melanin deposition in *Drosophila* eyes, we hypothesized that autophagic or lysosomal dysfunction may underlie the critical role of C99 in AD pathology. Using confocal microscopy and lysosome pH sensitive fluorescent markers, we demonstrated that *Drosophila* lysosomes fail to degrade fibrillar protein aggregates, leading to oxidative stress and mitochondrial dysfunction—processes that were ameliorated

upon treatment with BHB. Furthermore, protein–protein interaction (PPI) analysis of C99-expressing *Drosophila* brains revealed multiple pathways affected by C99, providing mechanistic insights into its pathogenic effects. Machine learning approaches further implicated protein phosphatase methylesterase-1 (PPME1) activation as a driver of C99-induced autophagic impairment. Finally, mathematical similarity analysis of PPI networks in C99-expressing *Drosophila* brains treated with either BHB or an mTOR inhibitor suggested that BHB may exert its neuroprotective effects through mTOR inhibition, potentially serving as a natural regulator of AD-related pathology.

Materials and methods

Drosophila Stocks

The following *Drosophila* stocks were used in this study, maintained under a 12-hour light/12-hour dark cycle at 60% relative humidity: GMR-Gal4 (BDSC #1104), UAS-BACE1 (BDSC #29877), UAS-C99 (BDSC #33784), UAS-A β 42 (BDSC #33769), UAS-APP (BDSC #33796), UAS-APP+BACE1 (BDSC #33797), UAS-APOE4 (BDSC #76607), tim-GAL4 (BDSC #7126), UAS-LC3-GFP (BDSC #8730), UAS-mito-QC (BDSC #91641), elav2-mito-Timer (fluorescent group consistent with BDSC #57323) and Gal80^{ts}; nSyb-Gal4/Tm6B (driver consistent with BDSC #39171). These stocks were either generated, maintained, or provided by Ms. Louise O’Keefe for this study.

Drosophila Treatment

For this study, AD *Drosophila* models were generated by expressing human APP and BACE1 under the vitreous GMR-Gal4 driver. Flies were maintained at 18°C until eclosion, after which adults were transferred to 25°C to initiate gene expression and treatment. BHB (2 mM, Sigma Aldrich, Cat. #: H6501) and saracatinib (Sara, 110 ng/ml, Sigma Aldrich, Cat. #: SML3195) treatments were administered by transferring larvae to supplemented food for and treat at least 10 days after emergence.

***Drosophila* eye analysis**

Fly eye images were collected and preprocessed to extract morphological features relevant to phenotypic classification. Specular reflections and glare were removed using inpainting techniques in HSV and LAB color spaces. Morphological features were extracted through grayscale conversion, histogram equalization, edge detection, and morphological closing. The processed images were resized to 128×128 pixels and converted to three-channel format to align with the input requirements of convolutional neural networks (CNNs). Data augmentation, including random brightness and contrast adjustments as well as horizontal flipping, was applied to improve model generalization.

A CNN model was constructed to predict phenotypic grades from extracted features. The architecture consisted of three convolutional layers (3×3 kernels) with ReLU activation and L2 regularization ($\lambda=10^{-4}$), each followed by max-pooling layers. A fully connected layer with 128 units and a dropout layer (rate=0.5) was included to mitigate overfitting, and a linear activation function was applied in the output layer for regression. The model was optimized using Adam with mean squared error (MSE) loss. Training was performed over 100 epochs with a batch size of 16.

To ensure robust evaluation, K-fold cross-validation (K=76) was employed. The dataset was randomly partitioned, with the model trained on K-1 folds and validated on the remaining fold in each iteration. Mean absolute error (MAE) was used to assess predictive performance, and the final results were averaged across all folds. Predicted labels, true labels, image filenames, and genotypic information were recorded for further analysis.

Transmission Electron Microscopy

Adult *Drosophila melanogaster* (3–5 days old) were anesthetized in cold phosphate-buffered saline (PBS) and dissected under a stereomicroscope. Head tissues were immediately fixed in 4% paraformaldehyde, 1.25% glutaraldehyde (EM grade), and 4% sucrose (pH 7.2) at 4°C overnight. Samples were rinsed twice in PBS with 4% sucrose (10 min each) and post-fixed in 2% osmium tetroxide (OsO₄) for 45 min at room temperature to enhance membrane contrast.

Dehydration was performed using an ethanol gradient (70%, 95%, 100%), with each step repeated three to four times for 10 min. Resin infiltration was carried out by incubating

samples in a 1:1 mixture of 50% propylene oxide (PPO) and 50% resin at room temperature for 1 hour, followed by immersion in 100% resin overnight. Polymerization was conducted at 70°C for 48 hours. Ultrathin sections (~70 nm) were obtained using an ultramicrotome and mounted on copper grids. Sections were double-stained with 2% uranyl acetate and 0.5% lead citrate to enhance contrast. Imaging was performed using a Cryo-TEM FEI Glacios 200 kV Cryo-Transmission Electron Microscope at 4800× magnification, focusing on photoreceptor cells in the *Drosophila* eye.

Mitochondrial segmentation was performed using ilastik (v1.4.0), leveraging a pre-labeled dataset from the Segmentation of mitochondria in EM images, which provides dense annotations of neuron membranes, synapses, mitochondria, and glial/extracellular space. The first image stack, containing manual expert annotations, was used to train the segmentation model.

Within ilastik Pixel Classification workflow, the pre-labeled mitochondrial regions served as ground truth, enabling supervised training of a Random Forest classifier. The classifier was trained on intensity, edge, and texture features at multiple scales to distinguish mitochondria from surrounding cellular structures. After training, the model was applied to the entire dataset to generate probability maps, which were thresholded to produce binary segmentation masks.

Post-processing was conducted using OpenCV to refine the segmented mitochondrial structures. Contours were detected, and morphological parameters such as size, shape, and spatial distribution within photoreceptor cells were quantified. To further investigate lysosomal abnormalities in AD *Drosophila* models, we applied an area-based thresholding approach to identify vesicles with size distributions similar to lysosomes. Vesicular structures were segmented, their areas were measured, and those falling within the predefined lysosomal range were selected for further analysis. The final segmentation results, including both mitochondria and lysosome-like vesicles, were overlaid onto the original TEM images for visualization and validation.

Fluorescent Imaging of *Drosophila* Eyes

Drosophila were anesthetized at 4°C for 10 minutes or exposed to CO₂ for 15 minutes, ensuring immobilization during imaging. Flies were affixed to glass slides with double-sided tape, positioning their heads upward to expose the eye region. Sample preparations were conducted under low-light conditions to prevent premature fluorescence excitation and maintain viability.

Fluorescent imaging was performed using a LEICA fluorescence microscope (Germany) with optimized settings for GFP (excitation: 488 nm, emission: 510 nm) and mCherry (excitation: 587 nm, emission: 610 nm). To maximize contrast, GFP and mCherry signals were acquired independently using sequential imaging. For extended observation, flies were re-anesthetized with CO₂ as needed and returned to fresh medium after imaging to maintain viability for longitudinal studies.

For mito-QC fluorescence in AD *Drosophila* models, standard dual-fluorescence exposure settings yielded minimal contrast between target fluorescence and the fluorescent background, hindering segmentation. To address this, we manually overexposed the fluorescent background to enhance the distinction between target fluorescence and background areas.

Fluorescent spots in *Drosophila* eye images were detected using K-means clustering ($K = 2$) combined with morphological closing and region-based feature analysis). Pseudopupil regions were automatically excluded, while fluorescence signals were quantified by computing the ratio of target fluorescence to the background-corrected fluorescence:

$$\frac{\Delta A}{\Delta B}$$

where A represents the fluorescence that exists in the natural state within the dual-fluorescence system, specifically mCherry in the case of mito-QC and green fluorescence in the case of mito-Timer. This calculation allows for an increase in quantitative values, demonstrating phenotypic improvements in *Drosophila*.

Gene Ontology enrichment

To elucidate the functional implications of differentially expressed genes (DEGs) in AD, Gene Ontology (GO) enrichment analysis was conducted using BiNGO (v3.10.3), a Cytoscape plugin for functional annotation. The analysis aimed to identify overrepresented biological processes, molecular functions, and cellular components associated with AD pathogenesis.

The input gene set comprised DEGs identified with an adjusted p-value < 0.05 and a fold-change threshold of [specify cutoff]. The background gene set included all expressed genes in the dataset to mitigate selection bias. GO term enrichment was assessed using a hypergeometric test, with p-values adjusted for multiple comparisons using the Benjamini–Hochberg false discovery rate (FDR) method. Terms with an FDR-adjusted p-value < 0.05 were considered statistically significant.

To facilitate biological interpretation, functionally related GO terms were clustered using the Markov Cluster Algorithm (MCL) implemented within BiNGO. The results were further integrated into an enrichment map in Cytoscape, enabling a network-based visualization of GO term relationships. This approach allowed identification of major functional modules implicated in AD, providing a systems-level perspective on the underlying molecular mechanisms.

Support Vector Machine

This study utilized gene expression data (GEO #GSE5281) to identify key AD-related genes through an integrated machine learning approach. We employed random forest, support vector machine (SVM), and autoencoder-based feature extraction, generating gene importance scores for downstream proteomic analysis. The dataset was normalized to ensure uniform feature scaling and stratified into balanced training and test sets. A random forest model (scikit-learn RandomForestClassifier) ranked genes based on feature importance, selecting the top 500 most relevant genes³². These genes were then processed using a deep autoencoder neural network (Keras) to extract compressed feature representations via a bottleneck layer, enhancing classification efficiency³³.

Following feature extraction, a linear kernel SVM was trained on the compressed dataset, with training repeated 100 times to obtain stable gene weight estimates³⁴. The average weight

for each gene across iterations was calculated to identify significant contributors to AD classification. Model performance was assessed by generating Receiver Operating Characteristic (ROC) curves, and the area under the curve (AUC) was used as a metric for classification accuracy.

To integrate transcriptomic and proteomic data, we mapped gene weights from classification models to AD protein datasets by aligning gene symbols with proteins identified in mass spectrometry experiments. This generated a set of protein scores reflecting transcriptomic importance in AD classification, enabling network-based functional analysis.

Immunoprecipitation

This study utilized co-immunoprecipitation (CO-IP) and protein extraction to analyze protein interactions in AD *Drosophila* models. For each genotype or treatment condition, two *Drosophila* heads were homogenized in pre-chilled 1X RIPA buffer supplemented with protease and phosphatase inhibitors. The homogenates were sonicated briefly and incubated on ice for 30 minutes, with vortexing every 10 minutes to enhance lysis. Following incubation, lysates were centrifuged at 14,000 rpm for 10 minutes at 4°C, and the clarified supernatants were collected in pre-chilled microcentrifuge tubes.

CO-IP was performed using the Catch and Release v2.0 Immunoprecipitation Kit (Upstate, Cat. #17-500). Supernatants were incubated overnight at 4°C with an anti-C-terminal antibody (Sigma, Cat. #A8717), following the manufacturer's protocol with modifications to enhance binding efficiency. Specifically, *Drosophila* proteins, antibody, and binding resin were incubated together, allowing for optimized protein capture. Immune complexes were washed three times with pre-chilled wash buffer under gentle rotation at 4°C. Bound complexes were eluted using the provided elution buffer, and eluates were collected for subsequent analysis.

Mass Spectrometry Analysis

Protein samples were digested into peptides using trypsin (Sigma, Cat. #650279) for subsequent mass spectrometry (MS) analysis. Ice-cold acetone (-20°C) was added at a 4:1 volume ratio, and the mixture was vortexed gently to ensure uniform precipitation. Samples were incubated at -20°C for at least 1 hour or overnight. Following precipitation, proteins

were pelleted by centrifugation (12,000–15,000 rpm, 4°C, 10–15 min), and the supernatant was removed. The dried protein pellet was resuspended in 10 mM Tris buffer for MS analysis.

Sample preparation, liquid chromatography-mass spectrometry (LC-MS), and protein identification were performed at the Proteomics Centre, University of Adelaide.

Wasserstein distance for PPI

Protein-protein interaction (PPI) data was obtained from STRING (9606.protein.links.detailed.v12.0), which includes a full network with subscores per channel. Relevant numerical features—"coexpression," "experimental," "textmining," and "combined_score"—were extracted. Log transformation and z-score normalization were applied to mitigate dispersion and ensure comparability. Labels were assigned based on the median of the "combined_score" feature to ensure balanced classification. Class imbalance was addressed by computing class weights. A multi-layer perceptron (MLP) model was implemented using TensorFlow/Keras, consisting of fully connected layers with ReLU activation, batch normalization, and dropout for regularization. The model was compiled with the Adam optimizer and mean squared error loss function. Training was conducted with class weights to improve learning on imbalanced data. Performance was assessed using mean absolute error (MAE) curve analysis. The trained model was applied to predict interaction scores for SARA and BHB protein pairs, with Wasserstein distance used to compare score distributions.

Jaccard Similarity

GO terms were extracted from BiNGO output files for AD, beta-hydroxybutyrate (BHB), and SARA datasets. The extraction process identified GO terms across three categories: Biological Process, Molecular Function, and Cellular Component. Jaccard similarity was used to quantify overlap between GO term sets from AD, BHB, and SARA. This was calculated as:

$$J(A, B) = \frac{|A \cap B|}{|A \cup B|}$$

Where A and B are the sets of GO terms for two conditions. Additionally, unique AD-specific GO terms were compared to BHB and SARA to assess distinct functional changes. Similarity distributions were modeled using a Gaussian approximation centered on observed Jaccard similarity values. Histograms were generated to visualize distributions of GO term similarities across conditions.

Plotting and t-testing

Plotting and mathematical calculations are performed by Python. Statistical significance testing was conducted using independent t-tests. Visualization was performed using matplotlib and seaborn, where histograms and density plots were generated to depict similarity distributions..

Results

Rescue of phenotypic regression caused by C99 of BHB

To determine which biomarkers are critical in BHB-mediated neuroprotection and to elucidate its specific protein targets, we utilized the *Drosophila* eye-specific GMR driver to generate transgenic models expressing human amyloidogenic pathway components via the UAS-GAL4 system. Given that *Drosophila* APP does not efficiently generate cytotoxic species following BACE1 processing, this system provides an optimal platform to investigate the functional contributions of individual proteins²³.

Our findings revealed severe degenerative eye phenotypes. However, conventional methods for quantifying eye integrity, such as Flynotyper, exhibited limitations in distinguishing these structural defects, particularly in assessing melanin deposition²⁴. To overcome this challenge, we trained a Grad-CAM enabling a refined assessment of neurodegeneration²⁵. This model employs a convolutional neural network (CNN) to predict the severity of eye damage in flies from images, assigning a continuous damage score²⁶. It processes images to remove glare and extract morphological features, enhancing the analysis of structural abnormalities. Additionally, Grad-CAM visualization highlights the key image regions influencing the predictions, offering insights into potential genotype-phenotype associations. Figure 1A presents Grad-CAM heatmaps across different genotypic conditions, revealing spatial patterns of degeneration. The first column displays original eye images of *Drosophila*

expressing neurodegeneration-related genes, while the second column shows Grad-CAM activation maps, where blue regions indicate healthy tissue and red regions highlight degeneration. The third column overlays the heatmap onto the original image for clearer interpretation. In control flies (GMR-GAL4), the heatmap exhibits minimal activation, reflecting the absence of significant degeneration. In contrast, flies expressing APP, BACE1, and A β exhibit varying degrees of neurodegeneration, characterized by increased red signal intensity (Figure 1B,C). Notably, co-expression of APP and BACE1 (APP + BACE1) leads to widespread neurotoxicity, suggesting a synergistic effect in disease progression. Notably, while *Drosophila* expressing BACE1 or A β did not exhibit overt structural damage in terms of reduced eye size, they appeared to display a deeper eye pigmentation (Figure 1B-D). This effect was particularly pronounced in flies expressing BACE1, where our data also revealed a subtle reduction in eye dimensions. This mild size reduction may indicate a degree of developmental impairment, suggesting that BACE1 expression potentially affecting developmental pathways in the *Drosophila* eye²⁷.

Interestingly, BHB treated APP+BACE1 flies appears to reduce red signal intensity, indicating a partial neuroprotective effect (Figure 1B-D). However, this protection does not prevent overall structural degeneration but instead primarily mitigates melanin deposition in *Drosophila* eyes. These findings suggest that BHB modulates specific aspects of neurodegenerative pathology rather than broadly preserving tissue integrity.

Rescue of amyloid deposition by BHB

Our findings identify C99 as a major contributor to neurodegeneration in *Drosophila*. Previous studies have suggested that this fragment disrupts lysosomal ion transport channels, leading to alterations in lysosomal pH²⁸. Consistently, we observed extensive melanin deposition in *Drosophila* eyes, which serves as further evidence of lysosomal clearance defects. Notably, BHB treatment markedly attenuated this phenotype, suggesting that BHB may modulate lysosomal acidification, particularly in the context of C99-induced dysfunction in AD.

To investigate this hypothesis, we performed transmission electron microscopy (TEM) on resin-embedded sections of *Drosophila* eyes, allowing detailed visualization of organelle ultrastructure and microtubular changes. For organelle identification, we employed a pretrained segmentation model from BioImage.io for mitochondrial detection in EM images²⁹.

Given the highly atypical vesicular structures associated with AD pathology, we applied the Segment Anything model to isolate all membrane-bound vesicles with a threshold size below 5000—excluding fibrillar tangles—for further analysis as putative lysosomes³⁰.

In contrast to the well-defined mitochondrial and vesicular structures observed in control flies, mitochondria in AD *Drosophila* were largely unidentifiable and severely reduced in number, making it difficult to reliably assess their integrity via TEM (Figure 2A, B). To investigate the underlying cause, we employed mito-Timer, a fluorescent reporter that shifts from green to red upon exposure to reactive oxygen species (ROS), allowing us to assess mitochondrial health and turnover³¹. Our results revealed that in AD *Drosophila* eyes, functional mitochondria were not only drastically reduced but also highly clustered, explaining the difficulty in identifying healthy mitochondria under TEM (Figure 2E, H). However, mitochondrial distribution and viability were clearly influenced by BHB treatment. Fluorescence imaging demonstrated a significant increase in healthy mitochondria following BHB administration (Figure 2E, H). Interestingly, TEM analysis further revealed a striking redistribution of mitochondria: rather than localizing at the peripheral membrane as in untreated AD flies, mitochondria in BHB-treated flies were repositioned around the nuclear periphery and encapsulated by membrane structures, forming a large, aggregated architecture (Figure 2C). This suggests that BHB not only enhances mitochondrial viability but may also play a role in mitochondrial spatial organization and compartmentalization within the cell.

Our primary focus was on lysosomal nuclear autophagy. A key observation from TEM analysis was the presence of an excessive number of vesicles in AD *Drosophila* eyes. To further characterize this phenomenon, we examined LC3, a marker of autophagic vesicles, and found that LC3-GFP fluorescence intensity significantly increased in AD models, indicating elevated autophagosome formation (Figure 2F, I)^{32,33}. Notably, this effect was further amplified following BHB treatment, suggesting that both AD pathology and BHB exposure act as autophagy-inducing factors. However, TEM images revealed that these vesicles frequently contained fibrillar structures, a hallmark of insoluble aggregated proteins (Figure 2B) ². Given that amyloid- β (A β) deposits and tau fibrils share this characteristic morphology, their presence in vesicles suggests that pathological protein accumulation alters vesicle structure^{3,33}. A notable feature of these vesicles was their significantly enlarged size, a phenomenon linked to cumulative toxicity in previous studies (Figure 2D) ³⁴. To investigate the underlying mechanism of this accumulation, we employed the pH-sensitive MITO-QC dual-color fluorescence system, which reports lysosomal acidification by the quenching of

green fluorescence. In AD *Drosophila*, the lysosomal pH was elevated, preventing green fluorescence quenching, consistent with impaired acidification. BHB treatment rescued this defect, restoring lysosomal pH homeostasis (Figure 2G, J). Correspondingly, TEM analysis revealed that BHB-treated flies exhibited smaller vesicles devoid of fibrillar aggregates, further supporting its role in mitigating lysosomal dysfunction (Figure 2C, D).

Changes in C99-interacting proteins of BHB

To further investigate how C99 disrupts autophagic function and whether BHB directly counteracts C99 activity, we performed immunoprecipitation to isolate C99-interacting proteins in *Drosophila* lacking APP+BACE1 expression, as well as in AD *Drosophila* with and without BHB treatment. Mass spectrometry analysis identified the protein interactome of C99 under these conditions.

GO clustering revealed that C99 exerts widespread effects on multiple pathways, including nuclear function, protein binding, and various metabolic processes³⁵. Notably, BHB treatment significantly altered numerous pathways, indicating its capacity to modulate C99-driven dysregulation (Figure 3A). To systematically classify these pathway alterations, we employed MCL analysis to cluster GO terms differentially enriched between BHB-treated and untreated AD *Drosophila*, categorizing them into Biological Process (BP), Cellular Component (CC), and Molecular Function (MF) terms³⁶.

Our findings highlight that the primary pathways influenced by BHB involve transcription and translation, particularly along the axis linking the nucleus to ribosomal activity (Figure 3B). Additionally, metabolic pathways, predominantly those centered around mitochondrial function, were markedly affected. Most importantly, we identified substantial disruptions in hydrolase activity and ubiquitination—two key regulatory nodes in autophagy^{37,38}. Ubiquitination serves as a crucial initiator of autophagy, maintaining mitochondrial homeostasis, mitophagy, and lysosomal degradation, while hydrolases are central to lysosomal proteolytic function. The pronounced effects of BHB on these pathways strongly suggest that it directly counteracts C99-mediated autophagic dysfunction by restoring ubiquitination and lysosomal enzymatic activity.

To further evaluate the therapeutic potential of BHB and identify key protein targets for future research, we applied Support Vector Machine (SVM) classification to rank genes based on their contribution to distinguishing BHB-treated from untreated conditions³⁹. This

model utilizes machine learning and deep learning to analyze gene expression data related to AD. A convolutional neural network CNN-based autoencoder extracts meaningful features from the top 500 genes identified by a random forest classifier, followed by a support vector machine (SVM) to classify AD samples. The model assigns an importance score to each gene based on its contribution to classification, enabling the identification of key genes associated with AD.

Figure 3C presents the most important genes identified by SVM, ranked by their average SVM weights, where higher weights indicate greater importance in classification. The color scale represents statistical significance (*P*-value), with red indicating higher significance and blue denoting lower significance. The top-ranking gene, HNRNPUL2-BSCL2, exhibited the highest SVM weight (0.37), followed by OPTN (0.35), EFR3B (0.34), and VPS35 (0.34). Notably, genes such as DNAJC7 and BSCL2 displayed high statistical significance despite lower SVM weights, suggesting potential biological relevance. The model demonstrated robust performance on test data, yielding an area under the curve (AUC) of 0.92 (Figure 3D).

Among the identified proteins, four were present in our C99 interactome dataset. BCCIP (BRCA2 and CDKN1A interacting protein), a key regulator of genome stability, was the only protein unaffected by BHB treatment, indicating a BHB-independent role in C99-mediated pathology (Figure 3E). In contrast, PPME1, VPS35, and GLOD4—all critical regulators of autophagy—were significantly influenced by BHB. Notably, PPME1 exhibited particularly low statistical *p* value in our model, suggesting that it may serve as a core pathway through which C99 exerts its effects, potentially representing a routine target of C99-mediated autophagic disruption.

Pathway sharing between ketone bodies and SARA

To elucidate how BHB alters C99 interactions and functionality, we investigated potential shared pathways between BHB and previously identified regulatory factors. Prior studies have highlighted an interaction between C99 and V-ATPase, which is modulated by SARA, a well-characterized phosphorylation inhibitor, exerting regulatory effects on phosphorylation-dependent signaling pathways, particularly the AMPK/mTOR axis^{28,40}. V-ATPase was among the proteins that exhibited reduced interaction with C99 following BHB treatment, raising the possibility of a shared mechanism between BHB and SARA.

To test this hypothesis, we performed immunoprecipitation of C99-interacting proteins in AD *Drosophila* treated with SARA, followed by mass spectrometry analysis to identify proteins that exhibit altered interactions. Using mathematical modeling, we quantified the degree of overlap between BHB- and SARA-induced changes in C99-associated protein networks. This comparative analysis provided critical insights into the potential mechanistic convergence between BHB and SARA, further reinforcing the role of AMPK/mTOR signaling in modulating C99-mediated autophagic dysfunction.

GO clustering analysis revealed that while BHB and SARA interventions exhibited some differences in the specific pathways they influenced, their overall effects were largely convergent (Figure 4A)³⁵. Both treatments primarily altered pathways related to nuclear function, metabolic regulation, and protein binding, with nearly identical clustering patterns despite differences in pathway abundance. Notably, both interventions consistently affected C99 interactions through transcriptional and translational regulation, autophagy modulation, and metabolic processes (Figure 4B).

To quantitatively assess the functional similarity between BHB and SARA in the context of neurodegeneration, we employed PPI (protein-protein interaction) network analysis integrated with machine learning-based predictive modeling. This model employs a multi-layer perceptron (MLP) to analyze protein-protein interaction (PPI) data, using features such as coexpression and experimental scores⁴¹. The data undergoes log transformation and standardization to ensure stability, while a median-based threshold is used to generate classification labels. To address class imbalance, weighted loss functions are applied during training. The model is optimized with mean squared error loss, and its predictions help quantify protein interaction patterns, providing insights into potential functional relationships. Key interaction features—including coexpression, experimental evidence, text mining scores, and combined scores—were extracted and normalized using log-transformation followed by standardization to mitigate extreme dispersion.

To predict intervention-related functional similarity, we trained a multilayer perceptron (MLP) model, using a median binarization approach to discretize interaction scores and ensure balanced class distribution. Figure X(A) illustrates the distribution of predicted similarity scores between SARA and BHB, which strongly clustered toward 1, with a Wasserstein distance of 0.0872, confirming a high degree of overlap in the proteins and PPI networks affected by both interventions (Figure 4C).

Additionally, Figure 4 D-E depicts the distribution of GO term similarity scores between AD-related perturbations and those induced by treatment. The relatively low Jaccard similarity index suggests that both interventions induce distinct functional changes compared to the AD baseline. However, as shown in Figure X(C), when considering only GO terms that exhibited significant changes under BHB or SARA treatment, we observed high Jaccard indices for biological processes (0.8118), molecular functions (0.8930), and cellular components (0.8727). This indicates that while BHB and SARA may exert distinct overall effects, their primary functional targets are largely conserved, reinforcing the notion that both interventions modulate C99 interactions through shared regulatory mechanisms.

Discussion

Aberrant processing of APP contributes to AD pathology, with multiple biomarkers implicated in disease progression⁴². While BHB has been associated with neuroprotection through metabolic and autophagic regulation, its specific molecular targets in AD remain unclear. Our study provides critical insights into the molecular mechanisms underlying BHB-mediated neuroprotection in *Drosophila* models of AD, with a particular focus on its impact on C99-driven pathophysiology. By leveraging deep learning models, high-resolution imaging, and mass spectrometry-based interactome profiling, we have identified key proteins and pathways modulated by BHB.

APP, BACE1, APOE, and A β have been extensively characterized in mammalian models of AD, where they collectively drive neurodegeneration through amyloid plaque formation, synaptic dysfunction, neuroinflammation, and lysosomal impairment^{1,43}. APP, a transmembrane protein, undergoes sequential proteolytic cleavage, with β -secretase (BACE1) initiating the amyloidogenic pathway^{44,45}. This cleavage generates C99, which is further processed by γ -secretase to produce A β peptides. Accumulation of A β , particularly A β 42, has been widely implicated in AD pathology, contributing to plaque deposition and neuronal toxicity⁴⁶. BACE1 overexpression in murine models exacerbates amyloid pathology, promoting synaptic loss and cognitive decline, while APOE4 has been identified as a major genetic risk factor influencing A β clearance and aggregation^{47,48}.

Despite the established role of these proteins in AD, our findings indicate that in *Drosophila*, neurodegeneration is primarily driven by C99 and the combined expression of APP and BACE1, rather than by A β or BACE1 alone. This discrepancy underscores fundamental

differences between *Drosophila* and mammalian models. *Drosophila* lacks an endogenous pathway that spontaneously triggers AD-like pathology, and APP processing by BACE1 in flies does not generate the same toxic A β species observed in human neurons²³. This suggests that in the absence of A β -driven neurotoxicity, alternative mechanisms—such as C99-mediated lysosomal dysfunction—become the dominant pathological drivers.

Through Grad-CAM analysis, we demonstrated that BHB treatment selectively attenuates neurodegeneration-associated activation signals in *Drosophila* models co-expressing APP and BACE1. Rather than broadly preventing structural deterioration, BHB primarily modulates melanin deposition and lysosomal function, suggesting a targeted effect on autophagy-related pathways. The pronounced accumulation of melanin—a feature not typically observed in mammalian AD models—further supports the link between lysosomal dysfunction and autophagic impairment in neurodegeneration. Given that melanin deposition is cleared through lysosomal autophagy, its accumulation in *Drosophila* suggests that neurodegeneration is associated with a failure of this pathway^{23,49,50}. Previous studies have provided initial evidence that C99 disrupts autophagic flux, but our findings position this dysfunction as a central pathological feature rather than a secondary consequence^{6,28}. Our results also highlight lipid-derived metabolites, such as BHB, as key modulators of autophagy in the context of C99-mediated dysfunction, providing new mechanistic insights into the metabolic regulation of lysosomal homeostasis in AD.

Our study further reinforces the importance of mitochondrial and lysosomal homeostasis in AD by identifying BHB as a major regulatory factor under amyloidogenic stress. Using transmission electron microscopy (TEM) and fluorescence imaging, we found that BHB rescues mitochondrial viability and shifts its localization toward the nuclear periphery. Notably, this phenomenon aligns with evidence that mitochondria can directly interact with the nucleus, modulating chromatin organization and nuclear signaling. In cardiomyocytes, mitochondria have been observed entering the nucleus, triggering chromatin redistribution, while mitochondrial-nuclear contact sites have been implicated in prosurvival signaling and cholesterol dynamics^{51,52}. We propose that under extreme pathological conditions such as AD, BHB signaling accelerates or enhances this process, recruiting mitochondria to the nucleus as a protective mechanism to sustain cellular survival.

Furthermore, our analysis of lysosomal pH homeostasis reveals that BHB effectively counteracts C99-induced disruptions, restoring acidification and reducing the accumulation of fibrillar aggregates within autophagic vesicles. This aligns with previous findings that BHB facilitates the clearance of misfolded and aggregated proteins, supporting its proposed neuroprotective role in AD^{19,53,54}. Given that lysosomal pH dysregulation is a hallmark of AD pathology, impairing autophagic degradation and lysosomal dysfunction disrupts brain iron metabolism and mitochondrial stability, exacerbating neurodegeneration—the ability of BHB to restore lysosomal acidification suggests a crucial regulatory mechanism^{55–58}. Additionally, lysosomal pH influences A β precursor protein metabolism and autophagic efficiency, further linking BHB metabolism to proteostasis in AD^{58,59}. Together, these findings underscore the role of BHB in modulating mitochondrial and lysosomal function, reinforcing its therapeutic potential in mitigating AD pathology by enhancing cellular homeostasis under amyloidogenic stress.

Mass spectrometry-based interactome analysis revealed that C99 expression in *Drosophila* disrupts proteostasis by impairing ubiquitination and hydrolase activity, leading to defective protein degradation and the accumulation of misfolded proteins. This dysfunction aligns with prior findings that C99 perturbs multiple cellular clearance pathways, exacerbating proteotoxic stress^{6,7}. Our results indicate that BHB counteracts these disruptions by restoring key regulatory components of the protein degradation machinery, particularly in autophagic and lysosomal pathways.

Among the identified proteins, PPME1 emerged as a particularly significant target, exhibiting the lowest p-value, suggesting it may serve as a broadly relevant regulator in proteostasis. PPME1 is a phosphatase methylesterase implicated in protein turnover and cellular stress adaptation, and previous studies have reported that its modulation improves AD phenotypes and promotes A β clearance⁶⁰. This aligns with our findings that BHB treatment significantly alters PPME1 activity, further supporting its role in BHB-mediated neuroprotection. However, a limitation of our study is that attempts to generate *Drosophila* models with PPME1 inhibition resulted in non-viable phenotypes, preventing further validation of its specific contribution to the observed rescue effects.

In addition to PPME1, we observed significant modulation of VPS35 and GLOD4, two proteins essential for autophagy and lysosomal function. VPS35, a core component of the retromer complex, is crucial for endosomal trafficking and lysosomal hydrolase recycling, while GLOD4, a glyoxalase domain-containing protein, has been linked to oxidative stress

resistance^{61,62}. Their involvement suggests that BHB facilitates proteostasis not only by enhancing degradation pathways but also by reinforcing cellular defenses against oxidative damage. Collectively, these findings support the hypothesis that BHB exerts its neuroprotective effects through targeted modulation of autophagic clearance mechanisms, effectively mitigating C99-induced proteostatic imbalance.

Interestingly, while BCCIP was present in the C99 interactome, it has not been reported to our knowledge, and remained unaffected by BHB treatment, suggesting that certain aspects of C99-driven pathology persist despite intervention. BCCIP, known for its role in DNA damage response and chromatin remodeling, has been implicated in neuronal survival and genome stability⁶³. Its resistance to BHB modulation may indicate that C99 disrupts nuclear processes in a manner independent of metabolic regulation, highlighting a potential limitation of BHB's protective effects.

Previous studies have identified the mTOR inhibitor SARA as a pharmacological agent capable of dephosphorylating C99, thereby modulating autophagy and lysosomal function⁴⁰. To determine whether BHB shares this mechanism, we conducted a comparative mathematical analysis and found that BHB, like SARA, also acts as an mTOR inhibitor and have the ability to act as an inhibitor of C99 activation, suggesting a conserved regulatory pathway in C99-associated neurotoxicity.

A key distinction, however, is that BHB is an endogenous lipid-derived metabolite, whereas SARA is an exogenous pharmacological compound. This raises the intriguing possibility that lipid metabolism may play a fundamental role in mTOR regulation and proteostasis. Given that lipid metabolic dysfunction is increasingly recognized as an early pathological feature of AD, it is plausible that disruptions in lipid homeostasis contribute to mTOR dysregulation, exacerbating proteotoxic stress and neurodegeneration⁶⁴. These findings position BHB not only as a metabolic intervention but also as a potential endogenous modulator of mTOR activity, linking lipid metabolism to key neurodegenerative pathways.

Data availability

All data and code supporting the findings of this study are available upon reasonable request from the corresponding author. Due to the nature of the study, data are not publicly accessible but can be provided upon request for academic and research purposes.

Acknowledgements

The authors acknowledge the instruments and expertise of Microscopy Australia (ROR: 042mm0k03) at Adelaide Microscopy, University of Adelaide, enabled by NCRIS, university, and state government support.

The authors acknowledge the instruments and expertise of Adelaide Proteomics Centre, with special thanks to Associate Professor Tara Pukala for her invaluable guidance on mass spectrometry.

This research was made possible through the invaluable support of the Adelaide Drosophila community, the Drosophila Facility at the University of Adelaide, and its outstanding researchers, Professor Robert Richards and Dr. Louise O’Keefe. We also extend our heartfelt condolences to memory of Dr. Louise O’Keefe.

This manuscript was edited using Overleaf, incorporating suggestions from language models, including Writefull’s model and GPT-based models. AI-assisted tools were utilized to improve grammar, clarity, and academic style. All modifications were reviewed and accepted by the authors to ensure accuracy and adherence to the intended scientific meaning.

Funding

No funding was received towards this work.

Competing interests

The authors report no competing interests.

References

1. Kumar A, Sidhu J, Goyal A, Tsao JW. Alzheimer Disease. In: *StatPearls*. StatPearls Publishing; 2022. Accessed March 21, 2022. <http://www.ncbi.nlm.nih.gov/books/NBK499922/>
2. Clarke JR, Lyra E Silva NM, Figueiredo CP, et al. Alzheimer-associated A β oligomers impact the central nervous system to induce peripheral metabolic deregulation. *EMBO Mol Med*. 2015;7(2):190-210. doi:10.15252/emmm.201404183
3. Brier MR, Gordon B, Friedrichsen K, et al. Tau and A β imaging, CSF measures, and cognition in Alzheimer's disease. *Science Translational Medicine*. 2016;8(338):338ra66-338ra66. doi:10.1126/scitranslmed.aaf2362
4. Capone R, Tiwari A, Hadziselimovic A, et al. The C99 domain of the amyloid precursor protein resides in the disordered membrane phase. *Journal of Biological Chemistry*. 2021;296. doi:10.1016/j.jbc.2021.100652
5. Checler F, Afram E, Pardossi-Piquard R, Lauritzen I. Is γ -secretase a beneficial inactivating enzyme of the toxic APP C-terminal fragment C99? *J Biol Chem*. 2021;296:100489. doi:10.1016/j.jbc.2021.100489
6. Lauritzen I, Pardossi-Piquard R, Bourgeois A, et al. Intraneuronal aggregation of the β -CTF fragment of APP (C99) induces A β -independent lysosomal-autophagic pathology. *Acta Neuropathol*. 2016;132(2):257-276. doi:10.1007/s00401-016-1577-6
7. Pera M, Larrea D, Guardia-Laguarta C, et al. Increased localization of APP-C99 in mitochondria-associated ER membranes causes mitochondrial dysfunction in Alzheimer disease. *EMBO J*. 2017;36(22):3356-3371. doi:10.15252/embj.201796797
8. Chikahisa S, Shimizu N, Shiuchi T, Séi H. Ketone body metabolism and sleep homeostasis in mice. *Neuropharmacology*. 2014;79:399-404. doi:10.1016/j.neuropharm.2013.12.009
9. Fukao T, Mitchell G, Sass JO, Hori T, Orii K, Aoyama Y. Ketone body metabolism and its defects. *Journal of Inherited Metabolic Disease*. 2014;37(4):541-551. doi:10.1007/s10545-014-9704-9
10. Gómora-García JC, Montiel T, Hüttenrauch M, et al. Effect of the Ketone Body, D- β -Hydroxybutyrate, on Sirtuin2-Mediated Regulation of Mitochondrial Quality Control and the Autophagy–Lysosomal Pathway. *Cells*. 2023;12(3):486. doi:10.3390/cells12030486
11. Ari C, Kovács Z, Juhasz G, et al. Exogenous Ketone Supplements Reduce Anxiety-Related Behavior in Sprague-Dawley and Wistar Albino Glaxo/Rijswijk Rats. *Front Mol Neurosci*. 2016;9:137. doi:10.3389/fnmol.2016.00137

12. Wang R, Li JJ, Diao S, et al. Metabolic stress modulates Alzheimer's β -secretase gene transcription via SIRT1-PPAR γ -PGC-1 in neurons. *Cell Metab.* 2013;17(5):685-694. doi:10.1016/j.cmet.2013.03.016
13. Cunnane SC, Courchesne-Loyer A, St-Pierre V, et al. Can ketones compensate for deteriorating brain glucose uptake during aging? Implications for the risk and treatment of Alzheimer's disease. *Ann N Y Acad Sci.* 2016;1367(1):12-20. doi:10.1111/nyas.12999
14. Liśkiewicz D, Liśkiewicz A, Nowacka-Chmielewska MM, et al. Differential Response of Hippocampal and Cerebrocortical Autophagy and Ketone Body Metabolism to the Ketogenic Diet. *Front Cell Neurosci.* 2021;15. doi:10.3389/fncel.2021.733607
15. McCarthy CG, Chakraborty S, Singh G, et al. Ketone body β -hydroxybutyrate is an autophagy-dependent vasodilator. *JCI Insight.* 2021;6(20). doi:10.1172/jci.insight.149037
16. Shippy DC, Evered AH, Ulland TK. Ketone body metabolism and the NLRP3 inflammasome in Alzheimer's disease. *Immunological Reviews.* 2024;n/a(n/a). doi:10.1111/imr.13365
17. Yamanashi T, Iwata M, Shibushita M, et al. Beta-hydroxybutyrate, an endogenous NLRP3 inflammasome inhibitor, attenuates anxiety-related behavior in a rodent post-traumatic stress disorder model. *Sci Rep.* 2020;10(1):21629. doi:10.1038/s41598-020-78410-2
18. Wu X, Gong L, Xie L, et al. NLRP3 Deficiency Protects Against Intermittent Hypoxia-Induced Neuroinflammation and Mitochondrial ROS by Promoting the PINK1-Parkin Pathway of Mitophagy in a Murine Model of Sleep Apnea. *Front Immunol.* 2021;12. doi:10.3389/fimmu.2021.628168
19. Versele R, Corsi M, Fuso A, et al. Ketone Bodies Promote Amyloid- β 1–40 Clearance in a Human in Vitro Blood–Brain Barrier Model. *Int J Mol Sci.* 2020;21(3):934. doi:10.3390/ijms21030934
20. Findlay JA, Hamilton DL, Ashford MLJ. BACE1 activity impairs neuronal glucose oxidation: rescue by beta-hydroxybutyrate and lipoic acid. *Front Cell Neurosci.* 2015;9:382. doi:10.3389/fncel.2015.00382
21. Lee AK, Kim DH, Bang E, Choi YJ, Chung HY. β -Hydroxybutyrate Suppresses Lipid Accumulation in Aged Liver through GPR109A-mediated Signaling. *Aging Dis.* 2020;11(4):777-790. doi:10.14336/AD.2019.0926
22. Busson D, Pret AM. GAL4/UAS targeted gene expression for studying Drosophila Hedgehog signaling. *Methods Mol Biol.* 2007;397:161-201. doi:10.1007/978-1-59745-516-9_13
23. O'Keefe L, Denton D. Using Drosophila Models of Amyloid Toxicity to Study Autophagy in the Pathogenesis of Alzheimer's Disease. *Biomed Res Int.* 2018;2018:5195416. doi:10.1155/2018/5195416

24. Ray J, Banerjee D, Wang Q, Girirajan S. Flynotyper 2.0: an updated tool for rapid quantitative assessment of *Drosophila* eye phenotypes. *G3 Genes/Genomes/Genetics*. 2024;14(11):jkae212. doi:10.1093/g3journal/jkae212
25. Selvaraju RR, Cogswell M, Das A, Vedantam R, Parikh D, Batra D. Grad-CAM: Visual Explanations from Deep Networks via Gradient-based Localization. *Int J Comput Vis*. 2020;128(2):336-359. doi:10.1007/s11263-019-01228-7
26. Sharma N, Jain V, Mishra A. An Analysis Of Convolutional Neural Networks For Image Classification. *Procedia Computer Science*. 2018;132:377-384. doi:10.1016/j.procs.2018.05.198
27. Jeon Y, Lee S, Shin M, et al. Phenotypic differences between *Drosophila* Alzheimer's disease models expressing human A β 42 in the developing eye and brain. *Anim Cells Syst (Seoul)*. 2017;21(3):160-168. doi:10.1080/19768354.2017.1313777
28. Im E, Jiang Y, Stavrides PH, et al. Lysosomal dysfunction in Down syndrome and Alzheimer mouse models is caused by v-ATPase inhibition by Tyr682-phosphorylated APP β CTF. *Sci Adv*. 2023;9(30):eadg1925. doi:10.1126/sciadv.adg1925
29. Gerhard S, Funke J, Martel J, Cardona A, Fetter R. Segmented anisotropic ssTEM dataset of neural tissue. Published online 2013:0 Bytes. doi:10.6084/M9.FIGSHARE.856713.V1
30. Kirillov A, Mintun E, Ravi N, et al. Segment Anything. Published online April 5, 2023. doi:10.48550/arXiv.2304.02643
31. Hernandez G, Thornton C, Stotland A, et al. MitoTimer: a novel tool for monitoring mitochondrial turnover. *Autophagy*. 2013;9(11):1852-1861. doi:10.4161/auto.26501
32. Baisamy L, Cavin S, Jurisch N, Diviani D. The Ubiquitin-like Protein LC3 Regulates the Rho-GEF Activity of AKAP-Lbc. *The Journal of Biological Chemistry*. 2009;284(41):28232. doi:10.1074/jbc.M109.054668
33. Gauthier S, Feldman HH, Schneider LS, et al. Efficacy and safety of tau-aggregation inhibitor therapy in patients with mild or moderate Alzheimer's disease: a randomised, controlled, double-blind, parallel-arm, phase 3 trial. *Lancet*. 2016;388(10062):2873-2884. doi:10.1016/S0140-6736(16)31275-2
34. de Araujo MEG, Liebscher G, Hess MW, Huber LA. Lysosomal size matters. *Traffic*. 2020;21(1):60-75. doi:10.1111/tra.12714
35. Ashburner M, Ball CA, Blake JA, et al. Gene Ontology: tool for the unification of biology. *Nat Genet*. 2000;25(1):25-29. doi:10.1038/75556
36. Azad A, Pavlopoulos GA, Ouzounis CA, Kyrpides NC, Buluç A. HipMCL: a high-performance parallel implementation of the Markov clustering algorithm for large-scale networks. *Nucleic Acids Res*. 2018;46(6):e33. doi:10.1093/nar/gkx1313
37. Barodia SK, McMeekin LJ, Creed RB, Quinones EK, Cowell RM, Goldberg MS. PINK1 phosphorylates ubiquitin predominantly in astrocytes. *NPJ Parkinsons Dis*. 2019;5:29. doi:10.1038/s41531-019-0101-9

38. Kaminsky V, Zhivotovsky B. Proteases in autophagy. *Biochim Biophys Acta*. 2012;1824(1):44-50. doi:10.1016/j.bbapap.2011.05.013
39. López OAM, López AM, Crossa DJ. Support Vector Machines and Support Vector Regression. In: *Multivariate Statistical Machine Learning Methods for Genomic Prediction [Internet]*. Springer; 2022. doi:10.1007/978-3-030-89010-0_9
40. Gubens MA, Burns M, Perkins SM, et al. A phase II study of saracatinib (AZD0530), a Src inhibitor, administered orally daily to patients with advanced thymic malignancies. *Lung Cancer*. 2015;89(1):57-60. doi:10.1016/j.lungcan.2015.04.008
41. Przybyła-Kasperek M, Marfo KF. A multi-layer perceptron neural network for varied conditional attributes in tabular dispersed data. *PLoS One*. 2024;19(12):e0311041. doi:10.1371/journal.pone.0311041
42. Olsson B, Lautner R, Andreasson U, et al. CSF and blood biomarkers for the diagnosis of Alzheimer's disease: a systematic review and meta-analysis. *Lancet Neurol*. 2016;15(7):673-684. doi:10.1016/S1474-4422(16)00070-3
43. Decourt B, Gonzales A, Beach TG, et al. BACE1 Levels by APOE Genotype in Non-Demented and Alzheimer's Post-Mortem Brains. *Current Alzheimer research*. 2013;10(3):309. doi:10.2174/1567205011310030010
44. Das U, Wang L, Ganguly A, et al. Visualizing APP and BACE-1 approximation in neurons yields insight into the amyloidogenic pathway. *Nat Neurosci*. 2016;19(1):55-64. doi:10.1038/nn.4188
45. Das B, Yan R. A Close Look at BACE1 Inhibitors for Alzheimer's Disease Treatment. *CNS Drugs*. 2019;33(3):251-263. doi:10.1007/s40263-019-00613-7
46. Gu L, Guo Z. Alzheimer's A β 42 and A β 40 peptides form interlaced amyloid fibrils. *J Neurochem*. 2013;126(3):305-311. doi:10.1111/jnc.12202
47. Jackson RJ, Hyman BT, Serrano-Pozo A. Multifaceted roles of APOE in Alzheimer disease. *Nat Rev Neurol*. 2024;20(8):457-474. doi:10.1038/s41582-024-00988-2
48. Dingwall C. A copper-binding site in the cytoplasmic domain of BACE1 identifies a possible link to metal homeostasis and oxidative stress in Alzheimer's disease. *Biochem Soc Trans*. 2007;35(Pt 3):571-573. doi:10.1042/BST0350571
49. Massey J, Wittkopp PJ. The genetic basis of pigmentation differences within and between *Drosophila* species. *Curr Top Dev Biol*. 2016;119:27-61. doi:10.1016/bs.ctdb.2016.03.004
50. Massey J, Wittkopp PJ. The genetic basis of pigmentation differences within and between *Drosophila* species. *Curr Top Dev Biol*. 2016;119:27-61. doi:10.1016/bs.ctdb.2016.03.004
51. Desai R, East DA, Hardy L, et al. Mitochondria form contact sites with the nucleus to couple prosurvival retrograde response. *Sci Adv*. 2020;6(51):eabc9955. doi:10.1126/sciadv.abc9955

52. Bakeeva LE, Skulachev VP, Sudarikova YV, Tsyplenkova VG. Mitochondria enter the nucleus (one further problem in chronic alcoholism). *Biochemistry (Mosc)*. 2001;66(12):1335-1341. doi:10.1023/a:1013374410540
53. Hood VL, Keller U, Haymond MW, Küry D. Systemic pH modifies ketone body production rates and lipolysis in humans. *Am J Physiol*. 1990;259(3 Pt 1):E327-334. doi:10.1152/ajpendo.1990.259.3.E327
54. Kashiwaya Y, Bergman C, Lee JH, et al. A ketone ester diet exhibits anxiolytic and cognition-sparing properties, and lessens amyloid and tau pathologies in a mouse model of Alzheimer's disease. *Neurobiol Aging*. 2013;34(6):1530-1539. doi:10.1016/j.neurobiolaging.2012.11.023
55. Roca-Agujetas V, Barbero-Camps E, de Dios C, et al. Cholesterol alters mitophagy by impairing optineurin recruitment and lysosomal clearance in Alzheimer's disease. *Mol Neurodegeneration*. 2021;16(1):15. doi:10.1186/s13024-021-00435-6
56. Santos JL, Petsidou E, Saraogi P, Bartsch U, Gerber AP, Seibt J. Effect of Acute Enriched Environment Exposure on Brain Oscillations and Activation of the Translation Initiation Factor 4E-BPs at Synapses across Wakefulness and Sleep in Rats. *Cells*. 2023;12(18):2320. doi:10.3390/cells12182320
57. Liu JL, Fan YG, Yang ZS, Wang ZY, Guo C. Iron and Alzheimer's Disease: From Pathogenesis to Therapeutic Implications. *Front Neurosci*. 2018;12:632. doi:10.3389/fnins.2018.00632
58. Chen Z, Zheng N, Wang F, et al. The role of ferritinophagy and ferroptosis in Alzheimer's disease. *Brain Research*. 2025;1850:149340. doi:10.1016/j.brainres.2024.149340
59. Schützmann MP, Hasecke F, Bachmann S, et al. Endo-lysosomal A β concentration and pH trigger formation of A β oligomers that potently induce Tau missorting. *Nat Commun*. 2021;12:4634. doi:10.1038/s41467-021-24900-4
60. Staniszewski A, Zhang H, Asam K, et al. Reduced Expression of the PP2A Methylesterase, PME-1, or the PP2A Methyltransferase, LCMT-1, Alters Sensitivity to Beta-Amyloid-Induced Cognitive and Electrophysiological Impairments in Mice. *J Neurosci*. 2020;40(23):4596-4608. doi:10.1523/JNEUROSCI.2983-19.2020
61. Wen L, Tang FL, Hong Y, et al. VPS35 haploinsufficiency increases Alzheimer's disease neuropathology. *The Journal of Cell Biology*. 2011;195(5):765. doi:10.1083/jcb.201105109
62. Utyro O, Włoczkowska-Łapińska O, Jakubowski H. Association of GLOD4 with Alzheimer's Disease in Humans and Mice. *J Alzheimers Dis*. 2024;101(3):823-834. doi:10.3233/JAD-240512
63. Lu H, Yue J, Meng X, Nickoloff JA, Shen Z. BCCIP regulates homologous recombination by distinct domains and suppresses spontaneous DNA damage. *Nucleic Acids Res*. 2007;35(21):7160-7170. doi:10.1093/nar/gkm732

64. Beel AJ, Sakakura M, Barrett PJ, Sanders CR. Direct Binding of Cholesterol to the Amyloid Precursor Protein: An Important Interaction in Lipid-Alzheimer's Disease Relationships? *Biochim Biophys Acta*. 2010;1801(8):975-982. doi:10.1016/j.bbalip.2010.03.008

Figure legends

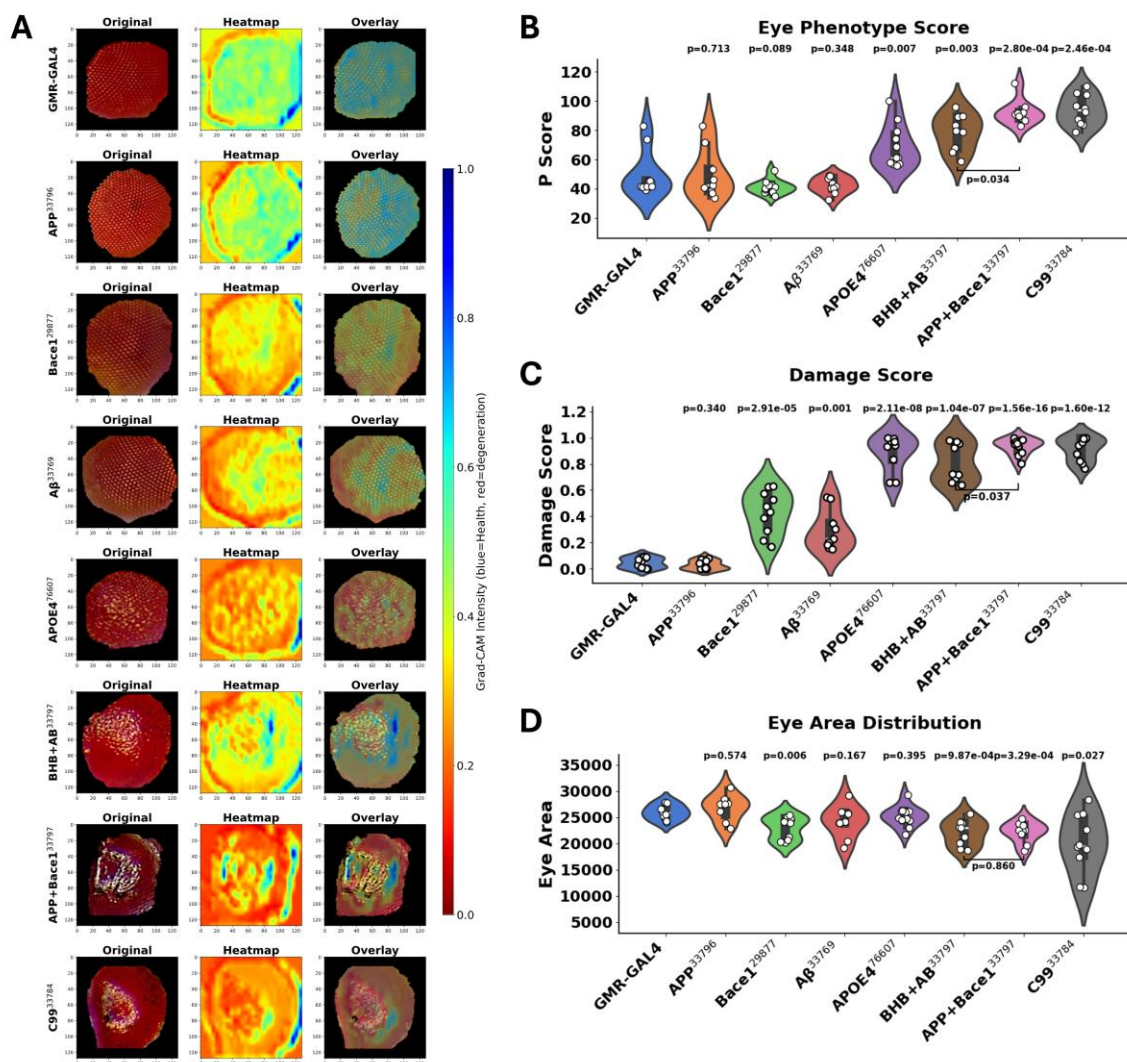


Figure 1 Grad-CAM analysis and quantitative assessment of neurodegeneration in *Drosophila* eye models. (A) Representative images of *Drosophila* eyes across different genetic backgrounds. For each genotype, the original eye image (left), Grad-CAM heatmap (middle), and overlay (right) are shown. The heatmap reflects pixel-wise Grad-CAM intensity, with red indicating neurodegeneration and blue indicating preserved regions. (B) Eye phenotype scores (P scores) quantified using Flynotyper. Compared to GMR-GAL4, APP, Bace1, A β , and APOE4 mutants show significantly altered scores. BHB treated APP+BACE1 (AB) and C99 mutants also exhibit significant deviations from controls. (C) Damage scores derived from image-based analysis of the Grad-CAM heatmaps. APP, Bace1, A β , and APOE4 mutants exhibit significantly increased damage compared to controls. Damage is further exacerbated in BHB + AB and APP + Bace1 combinations. Direct comparison between these two groups reveals a significant difference. (D) Eye area measurements indicate that APP, BHB + AB, and C99 mutants have significantly reduced eye sizes compared to controls. Violin plots display the distribution of values for each genotype, with individual data points overlaid. Wider regions indicate a higher density of data points. Sample sizes for all groups in (B–D): n=9–10 per genotype.

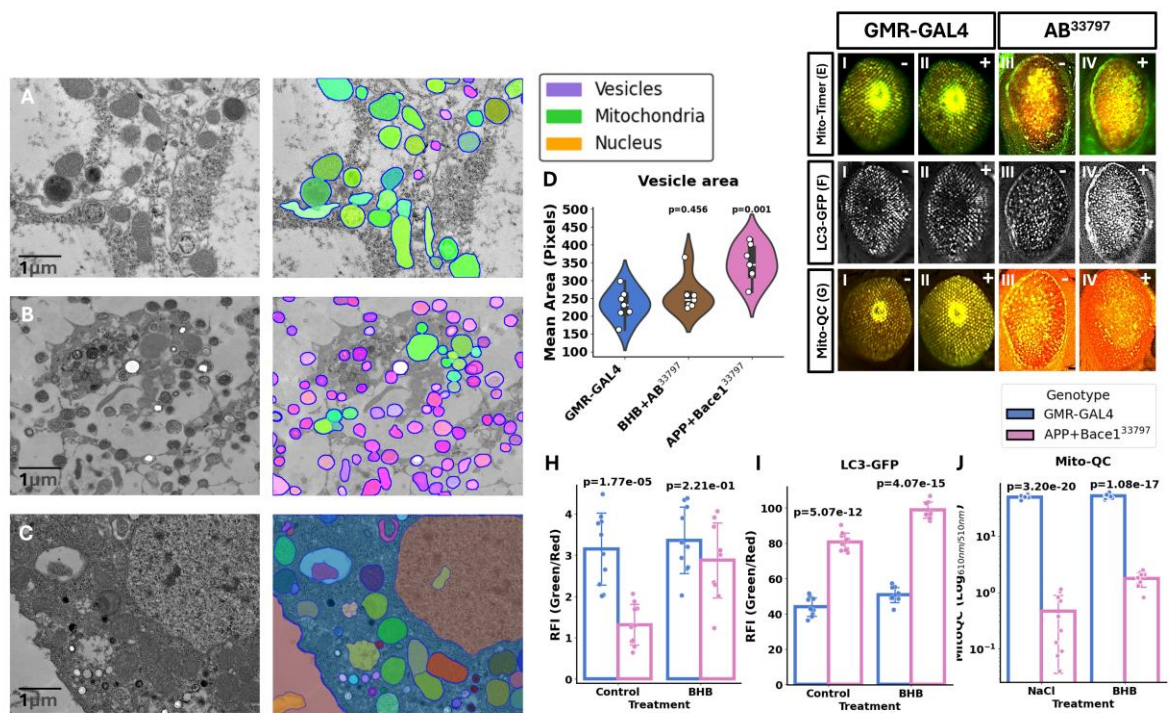


Figure 2 Ultrastructural and functional assessment of vesicles, mitochondria, and autophagy in *Drosophila* eye models. (A–C) Transmission electron microscopy (TEM) images of *Drosophila* retinal tissue from different genotypes, with corresponding segmentation highlighting vesicles (purple), mitochondria (green), and nuclei (orange). Other non-reference structures that are different from identifiable organelles are marked with different shades of these three colors according to their area. Scale bars, 1 μ m. (D) Vesicle area quantification based on TEM images. APP + Bace1 mutants exhibit a significant increase in vesicle size compared to GMR-GAL4, while BHB treated AD flies does not show a significant difference. Violin plots represent data distribution with individual data points overlaid. (E–G) Fluorescence images of *Drosophila* eyes expressing mitochondrial and autophagy-related reporters under different genetic backgrounds. The reporters include Mito-Timer (E), LC3-GFP (F), and Mito-QC (G), as indicated by the boxed labels. Panels I and II correspond to GMR-GAL4 flies, while panels III and IV correspond to APP + Bace1 flies. The “-” and “+” symbols denote untreated and BHB-treated conditions, respectively. (H) LC3-GFP fluorescence quantification as a measure of autophagic activity. BHB treatment significantly increases the relative fluorescence intensity (RFI, Green/Red) compared to controls. (I) Mito-Timer assay to assess mitochondrial turnover. BHB treatment leads to a significant reduction in the Green/Red fluorescence ratio, indicative of increased mitochondrial stress or degradation. (J) Mito-QC quantification, showing a significant reduction in mitochondrial quality control in BHB-treated groups compared to controls. Sample sizes for all quantifications (D, H–J): n=9–10 per condition. Statistical significance was assessed using Welch’s t-test.

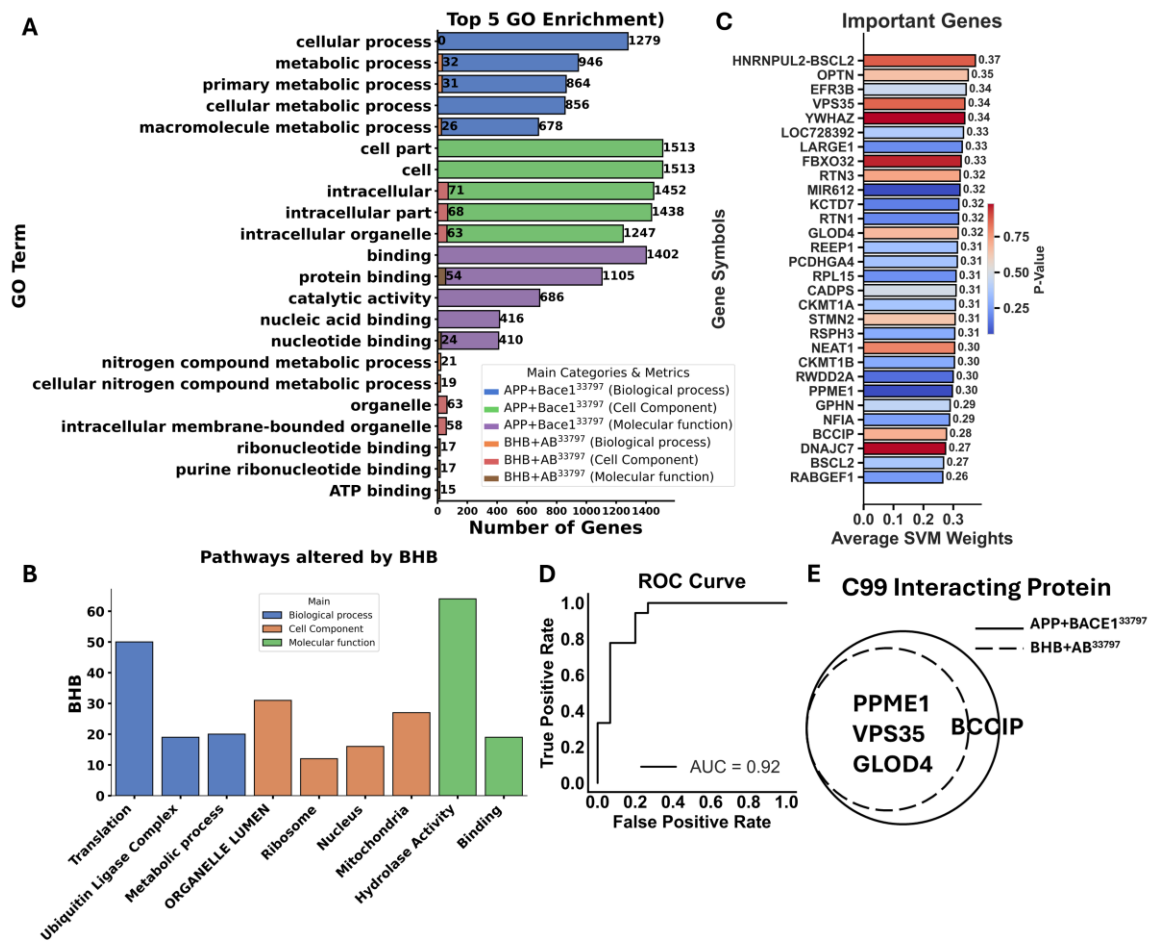


Figure 3 GO enrichment, key gene identification, and classification performance in BHB-treated *Drosophila* models. (A) Top 5 GO enrichment terms associated with differentially expressed genes (DEGs) across APP + Bace1 and BHB treated APP+BACE1 conditions. The bar graph shows the number of genes associated with each GO term, categorized into biological processes (blue), cellular components (purple), and molecular functions (pink). The five most enriched GO terms include cellular process, metabolic process, primary metabolic process, cellular metabolic process, and macromolecule metabolic process. (B) Pathways altered by BHB treatment, showing GO terms significantly enriched in BHB-treated conditions. Bars represent the number of genes associated with each category, classified into biological processes (blue), cellular components (orange), and molecular functions (green). Notably, BHB treatment alters pathways related to binding activity, mitochondrial processes, and hydrolysis activity. (C) Key genes identified by support vector machine (SVM) analysis. Genes with the highest average SVM weights are ranked, indicating their importance in distinguishing BHB-treated samples. HNRNPUL2-BSCL2, OPTN, and EFR3B are among the top-ranked genes. The p-value scale on the right suggests statistical significance in gene selection. (D) Receiver operating characteristic (ROC) curve evaluating the classification performance of the SVM model in distinguishing BHB-treated from control conditions. The area under the curve (AUC) = 0.92, indicating a high predictive accuracy. (E) Venn diagram of important proteins in flies treated with and without BHB. The dotted line represents flies treated with BHB, and the solid line represents the opposite.

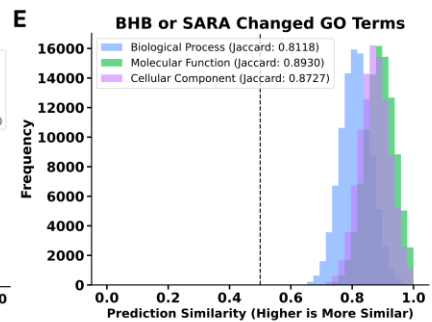
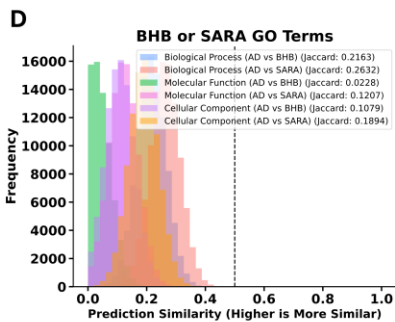
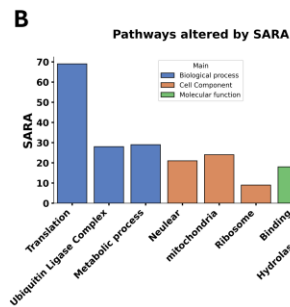
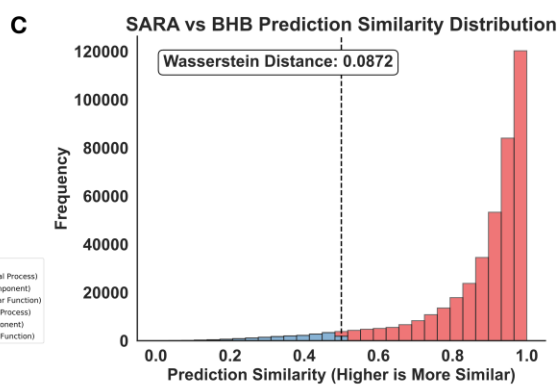
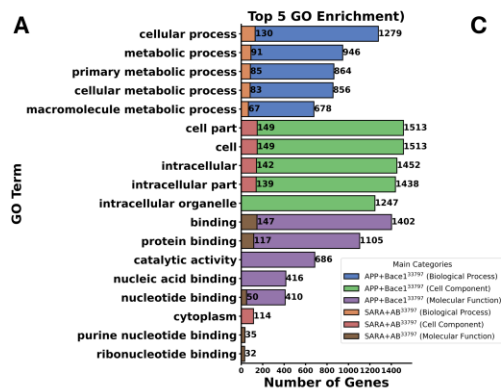


Figure 4 GO enrichment and comparative analysis of SARA- and BHB-associated pathways. (A) Top 5 GO enrichment terms associated with differentially expressed genes (DEGs) in APP + Bace1 and SARA treated APP + BACE1 conditions. The bar graph shows the number of genes associated with each GO term, categorized into biological processes (blue), cellular components (green), and molecular functions (purple). The five most enriched GO terms include cellular process, metabolic process, primary metabolic process, cellular metabolic process, and macromolecule metabolic process. (B) Pathways altered by SARA treatment, displaying significantly enriched GO terms. Bars represent the number of genes associated with each category, classified into biological processes (blue), cellular components (orange), and molecular functions (green). SARA primarily affects pathways related to binding activity, hydrolysis activity, mitochondrial function, and metabolic processes. (C) SARA vs. BHB prediction similarity distribution. Histogram showing the distribution of prediction similarity scores between SARA and BHB treatments, with a Wasserstein distance of 0.0872, indicating a high degree of similarity. (D) GO term comparison between BHB and SARA treatments. Histograms display the similarity distributions of biological processes, molecular functions, and cellular components between AD and BHB, as well as AD and SARA conditions, with corresponding Jaccard indices provided for each category. (E) Overlap of GO terms altered by BHB and SARA. High Jaccard similarity scores (biological process: 0.8118, molecular function: 0.8930, cellular component: 0.8727) suggest that BHB and SARA largely impact the same functional pathways.